Available online at www.sciencedirect.com

ScienceDirect

Procedia Structural Integrity 42 (2022) 1249–1258

Structural Integrity Procedia

www.elsevier.com/locate/procedia

23 European Conference on Fracture - ECF23

Nanosized SiC particle reinforced Ti6Al4V matrix composites manufactured by laser melting deposition

Yuyu Liu[a,b], Zheng Chen[a]*, Jianying He[b]

[a]*School of Material Science and Engineering, China University of Mining and Technology, Xuzhou 221116, China*
[b]*Department of Structural Engineering, Norwegian University of Science and Technology, Trondheim 7491, Norway*

Abstract

In this work, in-situ (TiC+Ti_5Si_3)/Ti6Al4V matrix composites (TMCs) with enhanced hardness and wear performance were manufactured by laser melting deposition (LMD) via the addition of nanosized SiC powder. The microstructures of single tracks were investigated to determine the optimal parameters for LMD. Besides, the influence of the SiC content on the microstructural evolutions and mechanical properties was explored. Results demonstrate that the in-situ reaction occurs between SiC and titanium during the LMD process. In-situ TiC and Ti_5Si_3 were distributed uniformly at grain boundaries and titanium matrix with a full-columnar grains for 0.5 wt.% and 1.0 wt.% SiC addition. The morphology of the composites consists of equiaxed grains with a three-dimensional quasi-continuous network structure when the content of SiC increases to 1.5 wt.% and 3.0 wt.%. The hardness of the composites is 321.1, 342.3, 347.8, and 442.1 Hv with the increasing formation of reinforcements. Meanwhile, the average coefficient of friction decreases from 0.39 to 0.32 with the wear mechanism changing from abrasion to adhesive wear.

Keywords: Titanium matrix composite; Laser melting deposition; In-situ reaction; Hardness; Wear resistance.

*

*Corresponding author.
E-mial address: chenzheng1218@163.com

10.1016/j.prostr.2022.12.159

1. Introduction

Additive manufacturing (AM) can effectively and consecutively fabricate complex and near-net-shaped parts from metal powder with many advantages such as a faster development cycle and a more flexible process. It also meets the requirements of precision molding and high performance, especially for the complex shape parts and multi-material gradient functional parts. Currently, the most widely studied AM technologies include laser melting deposition (LMD), selective laser melting (SLM), and wire arc additive manufacturing (WAAM). Among these processes, LMD offers distinct advantages such as the benefits of small substrate deformation, changeable powder mixture ratio, and controllable cooling rate, as stated by Hu et al. (2017), Li et al. (2017), and Mahmood et al. (2020).

The molten pools of AM are characterized with the steep temperature gradients and cooling rate. Xu et al. (2017) and Bermingham et al. (2019) proposed that the prevailing solidification conditions favor epitaxial growth and the nucleation particles are insufficient ahead of the solid/liquid (S/L) interface. Thus, columnar grains are inevitably coarse and textured for titanium-based alloy during AM. It is a promising approach to overcome this challenge by alloying ceramics with titanium to form titanium matrix composites (TMCs) in LMD process. TMCs are characterized with higher specific strength, specific stiffness, wear resistance, thermal stability and high-temperature durability than the conventional monolithic matrix materials, as reported by Laoui et al. (2006), Hayat et al. (2019), and Huang et al. (2011). While ceramics present brittle features due to their high hardness, and some defects could be found at the interfaces between the ceramic phases and the metal matrix, as stated by Ding et al. (2017). Thus, it is important that the ceramic can react with titanium to ensure strong metallurgical bonding at the interfaces between reinforcements and Ti matrix during in-situ process. Hu et al. (2018) used in-situ LMD process to prepare TiB/Ti TMCs that exhibited superior wear resistance and strength. Niu et al. (2021) utilized B to obtain TiB/Ti-Fe alloy by LMD process. In-situ TiB promoted the formation of equiaxed grains and presented a three-dimension quasi-continuous network (3DQCN) structure. Cai et al. (2019) synthesized in-situ TiB/Ti6Al4V TMCs by SLM and improved wear resistant with the formation of TiB reinforcement. While, SiC ceramic has better tribological performance than boron or TiB_2 to satisfy severe friction and heavy load-bearing conditions. Das et al. (2010) prepared a Ti-SiC composite layer on titanium substrate to improve wear resistance. The composite coatings with hardness between 976 and 1167 H_V exhibited average wear rate between 5.91 and 6.60 × 10^{-4} $mm^3(Nm)^{-1}$. Gu et al. (2011) manufactured (Ti_5Si_3+TiC)/Ti TMCs with fine wear resistance and hardness by SLM. However, SiC ingredients with a mean particle size of 13 μm led to the coarse dendritic structure in the matrix.

In this work, the nanosized SiC was mixed with Ti6Al4V powder to fabricate in-situ (TiC+Ti_5Si_3)/Ti6Al4V TMCs with enhanced hardness and wear resistant performance via LMD process. Grain growth mechanism in the melt pool was primarily studied under the different processing parameters. In order to understand the effect of SiC content on the microstructure of TMCs, the in-situ reaction and its generated reinforcements (TiC, Ti_5Si_3) were analyzed. Besides, the influence of reinforcement on the morphological evolution were also discussed to realize grain control. Hardness and friction behavior of TMCs were conducted to reveal the relationship between SiC content and properties.

2. Experimental

2.1. Composition design and materials

The composition (mass ratio) was designed in 0.5 wt.%, 1.0 wt.%, 1.5 wt.%, and 3.0 wt.% SiC/Ti6Al4V, named as TMC1, TMC2, TMC3 and TMC4, respectively. The in-situ reaction between SiC and titanium can be given: $8Ti+3SiC \rightarrow Ti_5Si_3+3TiC$. The theoretical volume fraction of in-situ reinforcements can be calculated by the equation according to the reaction. The reaction formation enthalpy (ΔH) and Gibbs free energy (ΔG) of the reaction at high temperature were also calculated in Fig.1. The negative ΔH and ΔG theoretically imply the spontaneity of in-situ reaction during LMD process.

The raw materials include gas atomized Ti6Al4V powder (produced by Hangtian Haiying Co Ltd., China) and nanosized SiC powder (purchased from Aladdin Co Ltd., China), as shown in Fig. 2a and b. Ti6Al4V powder is near spherical shape with the diameter range of 10 ~ 50 μm and the average size of SiC particle is 40 nm. Different mass ratios of SiC and Ti6Al4V powders were weighted as Table 1 and then kept in vacuum at 80 ℃, 6 h for drying. Pure Ti6Al4V served as blank control. SiC and Ti6Al4V powders were mechanically blended for 6h to make spherical

Ti6Al4V enclosed by SiC nanoparticles. Fig. 2c shows that the surface of Ti6Al4V was uniformly coated by SiC for feeding during LMD deposition.

Table 1. The designed mass ratio and calculated theoretic volume fraction according to the in-situ reaction.

	Wt.%SiC	Vol.%Ti_3Si_5	Vol.%TiC
TMC1	0.5 wt.%	1.39 vol.%	0.67 vol.%
TMC2	1.0 wt.%	2.77 vol.%	1.33 vol.%
TMC3	1.5 wt.%	4.16 vol.%	1.99 vol.%
TMC4	3.0 wt.%	8.33 vol.%	4.00 vol.%

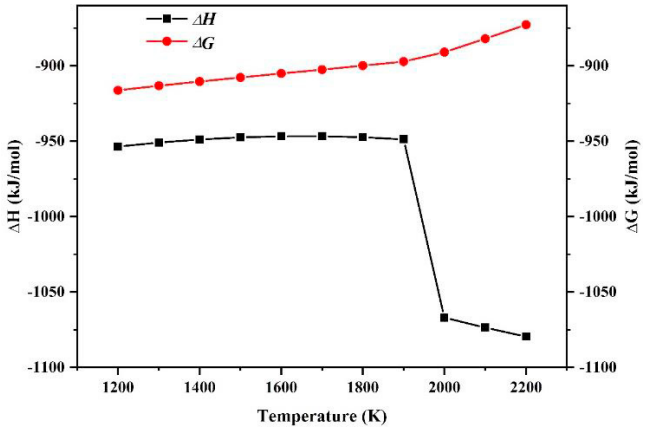

Fig. 1. The formation enthalpy and Gibbs free energy of in-situ reaction: 8Ti+3SiC→Ti_5Si_3+3TiC.

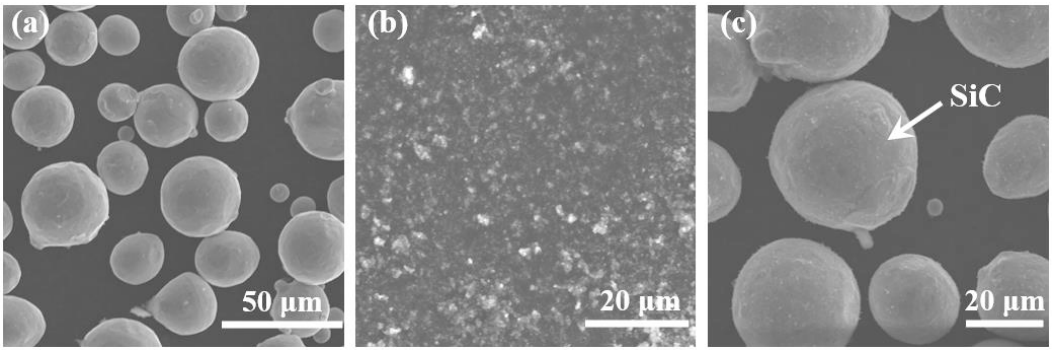

Fig. 2. (a) raw material of Ti6Al4V powder with diameter of 10 ~ 50 μm; (b) nanosized SiC powders with average size of 40 nm; (c) as-blended Ti6Al4V powder enclosed by nanosized SiC on the spherical surface.

2.2. LMD process of single tracks and multi-layers bulk

TMCs were built up by LMD equipment that consists of laser generator (YSL-3000 fiber laser, wavelength of 1.07 μm), printing chamber (protective gas Ar, O_2 below 200 ppm), powder and shield gas system, and numerical control. The substrate was chosen as a rolled Ti6Al4V plate with the size of 160×160×20 mm and the deposited surface was polished and cleaned. For the single-track cladding, nine tracks of TMC2 were deposited under different processing parameters including laser power (P, 1200, 1500, 1800 W), scanning speed (v, 360, 480, 600 mm/min), and feed rate (f, 3.6, 4.8, 6.0 g/min). The optimal parameter combination was given in the following analysis and used in the

subsequent multi-layer deposition. For the bulk, the S-shaped scanning path was used for fabrication and the printing direction between the successive rotation of 90°.

2.3. Microstructure characterization and properties

The samples along the building direction were first polished by 0.05 μm colloidal silica and followed by etching with Kroll's reagent (10% HF, 20% HNO_3, 70% H_2O) for 15 s. The microstructure of samples was observed by optical microscope (OM, Olympus-PMG3) and scanning electron microscope (SEM, Hitachi SU8220) equipped with energy dispersive spectrometry (EDS, Bruker, QUANTAX). The lattice structures were identified by X-ray diffractometry (XRD, Bruker D8 Advance) with monochromatic Cu Kα radiation.

The hardness of the samples was operated on a Vickers hardness machine (MH-50), with the diamond as the squeeze head. The load was 1 kg and kept for 10s. To assure accuracy, each sample was measured with 8-10 points for averaging. The friction and wear tests were conducted on a UMT friction tester with a pressure of 30 N, time of 60 min, rubbing route of 10 mm, and friction pair of Al_2O_3 grinding balls (diameter: 5 mm).

3. Result and discussion

3.1. Microstructure of single tracks and optimal processing parameters

Single track is the basic unit of LMD that build a part track-by-track and layer-by-layer. Figs. 3a-i exhibit the cross-section geometries of nine single tracks in the composition of TMC2 under different parameter combinations. The geometry features including height, width, depth, and dilution were collected in Fig. 3j. *w* of the tracks increases as *P* increase, but decreases as *v* and *f* increase, indicating that the parameters have a coupling effect on the geometry of the deposited layer.

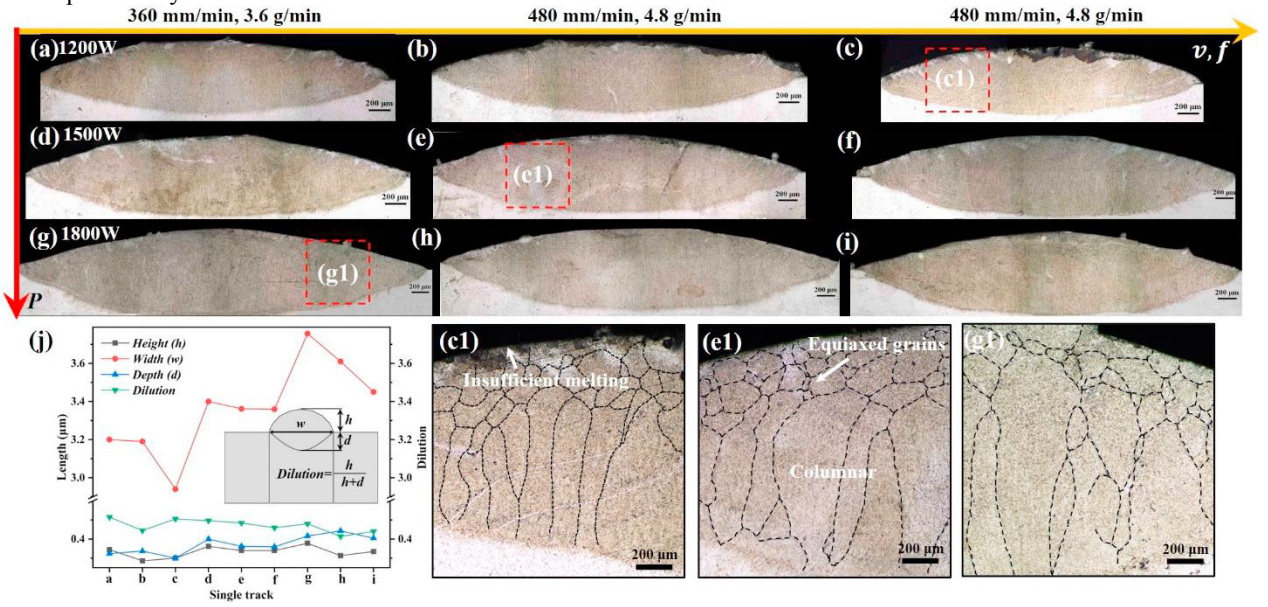

Fig. 3. (a-i) Cross-section geometries of nine single tracks of TMC2 under different deposited parameters. The yellow coordinate represents the scanning speed and feed rate, respectively, increasing from 360, 480, to 600 mm/min and 3.6, 4.8 to 6 g/min. The red coordinate represents the laser power that increase from 1200, 1500, to 1800 W; (j) the plot of geometry data including height, width, depth, and dilution for nine single tracks; (c1, e1 and g1) the OM insets after zooming in.

Dilution of a clad layer is defined as the ratio of cladding depth (d) to the sum of its height (h) and depth. In other words, it represents the extent of mixing between the clad material and the base material. Wang et al. (2015) explained that large dilution leads to high melt superheating, large penetration re-melting, and epitaxial growth. Thus, dilution should be appropriately small. The dilutions of the tracks under 1200W are larger than that of 1500 and 1800W. The detailed deposited tracks are depicted in Fig. c1, e1 and g1, indicating two grain growth mechanisms: columnar grain with epitaxial growth from the pool bottom and equiaxed grain with heterogenous nucleation. It is clear to see that the columnar grains coarsen and the number of equiaxed grains decrease with P increasing. While lower power leads to insufficient melting at the top of the melt pool as shown in Fig. 3c1. Therefore, the processing parameter of 1500W, 360 mm/min, and 6 g/min was determined and used for the subsequent multi-layer deposition.

3.2. Phase transformation and microstructural evolution

Fig. 4 shows the XRD patterns of Ti6Al4V and TMCs to reveal the in-situ phase transformation after deposition. As shown in Fig. 4a, all diffraction peaks of TMCs shift to the right for a maximum 0.6° compared with the XRD profile of Ti6Al4V. In particular, it is more obvious to see the detailed main peaks at around 42°. Detailed phase analysis is further shown in Fi. 4b. The result of Ti6Al4V demonstrates that the lattice parameters of α (hcp Ti) are determined as a=0.294 nm and c=0.467 nm, with β phase as a=0.32 nm. The diffraction peak of a small amount of retained β phase exists at 39.4° with (110) plane. The peaks of TiC and Ti_5Si_3 appear in the TMC4 pattern, with lattice constant of a=0.43 nm, and a=0.746 nm with c=0.516 nm, respectively, according to the PDF of TiC and Ti_5Si_3. It is interesting to note that TiC peaks of TMC4 slightly shift to the right compared to the standard PDF of TiC. Because C atom percentage ranges from 32 to 49 at. % in Ti-C binary phase diagram by Roger et al. (2017). The lattice constant of TMC4 is smaller than that of standard TiC corresponding to the (111) plane. Besides, more titanium atoms involve in in-situ reaction with addition of SiC increasing from 0.5 to 3.0 wt.%, leading to the right deviation. It indicates in-situ reaction occurs during the LMD process and in-situ TiC and Ti_5Si_3 reinforcements exist in the matrix.

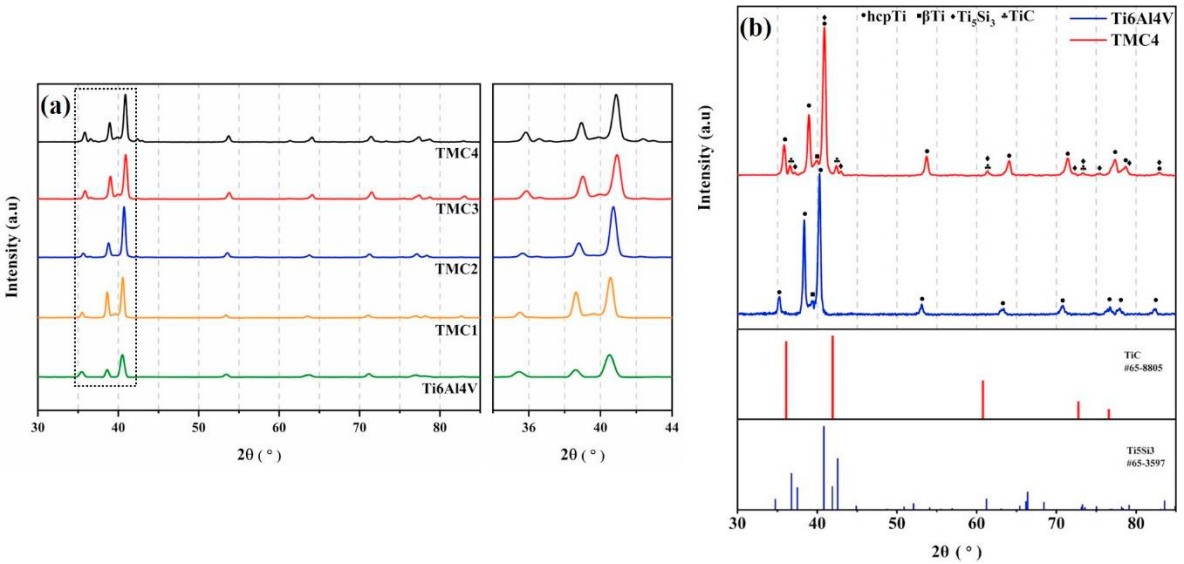

Fig. 4. (a) XRD patterns of Ti6Al4V and TMCs with the main peaks at around 40°; (b) the detailed patterns of Ti6Al4V and TMC4 with PDF of TiC and Ti_5Si_3.

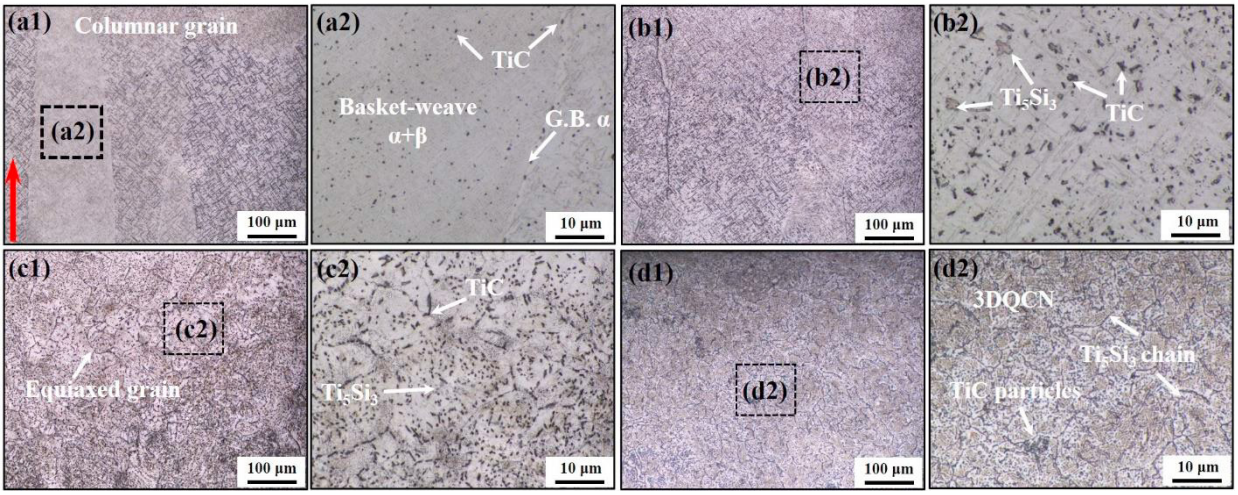

Fig. 5. OM images and magnified inset of TMCs. (a1-2) TMC1; (b1-2) TMC2; (c1-c2) TMC3; (d1-2) TMC4. (Red arrow refers to the deposition direction, the same building direction as below samples.)

Fig. 5 presents the OM images of TMCs by the LMD process. As shown in Fig. 5a1, the microstructure consists of coarse penetrating β grains along the deposition direction. In the magnified images within the prior β phase, it is delineated by α grain boundary and typical α+β basket weave morphology. Only small amounts of in-situ TiC were distributed in the matrix and α grain boundaries uniformly. Because the maximum solubility of Si and C in β-Ti are about 3 at.% and 0.8 at.%, respectively, a large number of Si atoms solubilize in the titanium alloy while the solubility between C and titanium is considerably tiny. The microstructure of TMC2 also shows the columnar grains with the in-situ reinforcements increasing to 2.77 and 1.33 vol.% as aforementioned. More in-situ Ti_5Si_3 and TiC were clearly observed inside the columnar in Fig. 5b2. The bright and white contrast regions refer to the Ti_5Si_3 phase and the dark counterparts are TiC, a similar result as Masaki et al. (2005). By SiC increasing to 1.5 wt.%, the transition from columnar to equiaxed occurs, as shown in Fig. 5c1. The distribution of the reinforcements is denser than that of TMC1 and TMC2. Increasing formation of in-situ reinforcements generates the quasi-continuous boundaries and tailors the matrix into a 3DQCN structure. Fig. 5d2 shows refiner grains and in-situ Ti_5Si_3 chain and granular TiC are cleaner at grain boundaries which can be verified by further element mapping.

Fig. 6 shows SEM images of TMCs with element distributions of the in-situ reinforcements. The white dotted line in Fig. 6a depicts the coarse prior β grains with typical duplex phases inside. The inset shows the detailed prior β grain boundary with the existence of the in-situ TiC. As shown in Fig. 5a2, the reinforcements also exist at α grain boundaries. Likewise, it is more evident to see the same phenomenon of TMC2 in Fig. 6b1 and b2. The reinforcements are diffusely distributed in the titanium alloy matrix in Fig. 6c1 and c2. As shown in EDS mappings of Fig. 6c3, the solubility between Al and C is poor and C element distribution proves the granular TiC reinforcement. When TiC phase is precipitated by the eutectic reaction, the growth pattern and growth rate on all crystal planes are the same. Thus, in-situ TiC is inclined to form the granular shape (2001). The microstructure of TMC4 is divided into reinforcement rich region and matrix region and form a 3DQCN structure, as shown in Fig. 6d2. Besides, the interface between the reinforcements and titanium matrix exhibits fine metallurgical bounding without pores, cracks, and deflects in Fig. 6d2. The EDS mappings of Fig. 6d3 present apparent Si and C agglomeration, demonstrating that Ti_5Si_3 is the chain-shaped phase and the granular phase is TiC.

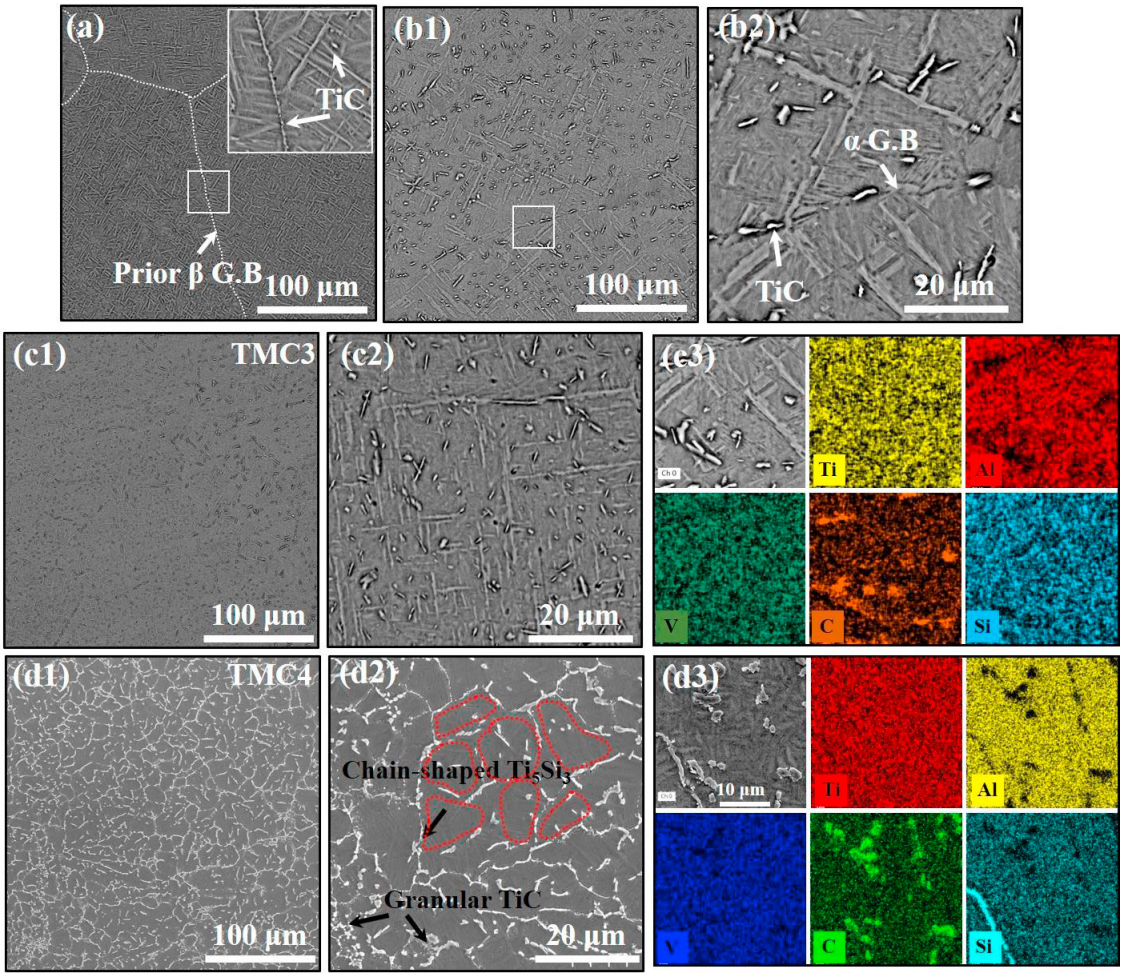

Fig. 6. SEM images of TMCs. (a) TMC1; (b1-2) TMC2; (c1-3) TMC3 with EDS mappings; (d1-3) TMC4 with EDS mappings.

The solidification mechanism and path can be discussed according to the aforementioned. According to the Ti-Si-C ternary phase diagram, the solidification sequence of the TMCs solidification during the LMD process is expected to be the following: (i) *Liquid* (*Ti+Si+C*); (ii) *Liquid* (*Ti+Si+C*) → *β-Ti* + *Liquid*$_1$; (iii) *Liquid*$_1$ →*β-Ti* + *eutectic-TiSi* + *eutectic-TiC*; (iv) *β-Ti* +*TiC* → *α-Ti*; (v) *β-Ti* → *α-Ti* + *Ti*$_3$*Si*. However, Ti_3Si phase only can be obtained under an extremely slow cooling process. In general, the phase of the eutectic transformation is Ti_5Si_3 verified by Fig. 4. For the solidification of LMD process, extremely high cooling speed make the first solidification steps occur in an ultrafast interval. In-situ reinforcements distribute at prior β grain boundaries as shown in Fig. 6a, which can act as the precipitates pinning on the boundaries to prevent the grain coursing. Moreover, the mismatch between close packed plane of $(110)_\beta$ and that of $(111)_{TiC}$ is about 7.3%, demonstrating TiC can be regarded as the potent heterogenous nucleation particles for β Ti. The mismatch between $(0001)_\alpha$ and $(0001)_{Ti5Si3}$ is calculated to be about 11%, which can efficiently promote grain refinement, according to the theory of Bramfitt (1999).

3.3. Hardness and friction behavior

Fig. 7 shows the relationship between the hardness and SiC content for in-situ ($TiC+Ti_5Si_3$)/Ti6Al4V. The initial hardness of Ti6Al4V is 300.9 Hv. With the increase of in-situ reinforcement formation, the hardness of TMCs rises to 321.1, 342.3, 347.8, and 442.1 Hv, respectively. The hardness is defined as the following: $Hv=P/A=\alpha P/d^2$, where P and A are the peak indentation load and the pyramidal contact area. α and d refer to the constant and length of the

diagonal of the resultant impression. As the OM insets shown, the indentation area decreases gradually as SiC content increases from 0 to 3 wt.%. The hardness of TiC and Ti_5Si_3 are 30 GPa (3061 Hv) and 11.3 GPa (1153 Hv) respectively, which is significantly higher than that of Ti6Al4V, demonstrating that the formation of in-situ reinforcements efficiently improves the hardness of the composites.

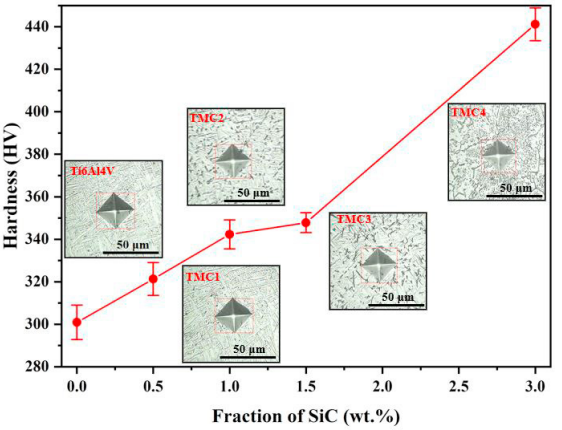

Fig. 7. Plot of Vickers Hardness against SiC addition content with indentation insets.

SEM images of wear tracks for in-situ (TiC+Ti_5Si_3)/Ti6Al4V are exhibited in Fig. 8. The worn surface of TMC1 reveals parallel furrows and grooves with many damaged surfaces and detached edges in Fig. 8a1. There are massive loose wear debris distributed on the wear track and EDX analysis (Point 1) of debris proves the presence of Si and C elements which can act as new peelings to accelerate wear failure. The characteristic morphology is considered to be abrasion wear for TMC1. Fig. 8b2 also shows some delaminated regions and rough worn layers. The composition of Point 2 indicates increasing Si content in the debris. As the SiC content increases to 1.5 wt.%, the worn track becomes smoother and the debris decrease in Fig. 8c1. The enlarged inset shows the worn surface is covered by a strain-hardened layer without damage and cracks with Si and C element composition increasing (Point 3), which indicates that the wear mechanism changes from abrasion to adhesive wear. It is obvious to see that the furrow surfaces are rather smooth with the elimination of delaminated regions. The harder in-situ reinforcements (TiC+Ti_5Si_3) may account for the decreasing spalling of the tribological layer.

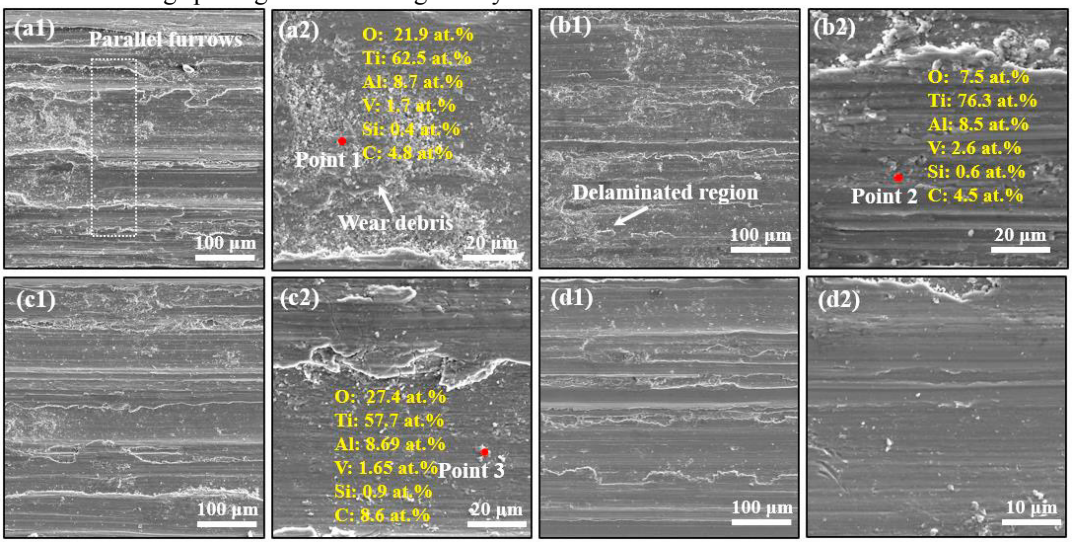

Fig. 8. The worn surfaces after friction test for TMCs with EDX analysis. (a) TMC1; (b) TMC2; (c) TMC3; (d) TMC4.

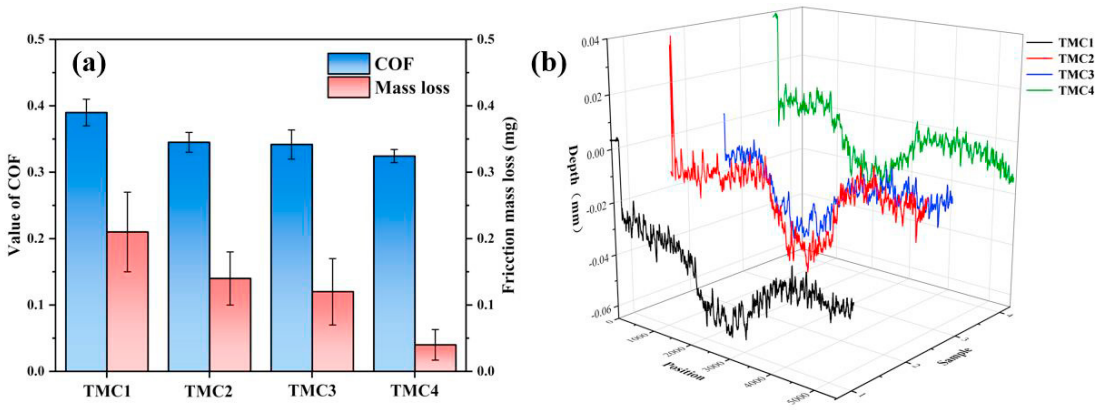

Fig. 9. (a) The coefficients of friction and mass loss; (b) depth of wear tracks for TMCs.

The COFs and mass loss are exhibited in Fig. 9a. The average COF values are 0.39, 0.345, 0.341, and 0.32 for TMC1-4, respectively. The mass loss of TMCs is 0.21, 0.14, 0.12, and 0.04 mg in the order. The mass loss of TMC4 is about 80% less than that of TMC1. The wear track of TMC1 is the deepest among the TMCs as shown in Fig. 9b. Wear resistance of TMCS is enhanced by increasing the addition of SiC ceramic. As aforementioned, in-situ TiC and Ti_5Si_3 phases is attributed to the reaction between SiC and Ti matrix, which are expected to exhibit chemical stability and compatibility with the matrix in Fig. 6d2. Besides, TiC and Ti_5Si_3 show the dispersed distribution in the titanium matrix that plays the role of dispersion strengthening effect at lower reinforcement fraction. Meanwhile, Huang et al. (2009) found that 3DQCN structure with refine morphology can blunt and deflect cracks, slow crack propagation, and bear the strain.

4. Conclusions

In-situ (TiC+Ti_5Si_3)/Ti6Al4V composites were fabricated by laser melting deposition (LMD) via the addition of nanosized SiC powder. Epitaxial growth and equiaxed grains exist in the melt pool. The geometries of single tracks were investigated to determine the optimal processing parameters of 1500W, 360 mm/min, and 6 g/min with the proper dilution. The in-situ reaction between SiC and titanium occurs in the melt pool and the formation of TiC and Ti_5Si_3 was verified. Granular TiC and chain-shaped Ti_5Si_3 facilitate heterogenous nucleation and promote the transition of columnar to equiaxed with a three-dimensional quasi-continuous network structure. By the addition of SiC increasing to 3.0 wt.%, the hardness of the composite is 442.1 Hv, which increases by 37.6% of that of TMC1. The average COFs are 0.39, 0.345, 0.341, and 0.32 and the wear mechanism changes from abrasion to adhesive wear with more in-situ reinforcements formation.

Acknowledgements

The authors are grateful for funding from the Natural Science Foundation of China (51771226).

References

Hu, Y., Zhao, B., Ning, F., Wang, H., Cong, W., 2017. In-situ ultrafine three-dimensional quasi-continuous network microstructural TiB reinforced titanium matrix composites fabrication using laser engineered net shaping. Materials Letters 195, 116–119.

Li, Y., Hu, Y., Cong, W., Zhi, L., Guo, Z., 2017. Additive manufacturing of alumina using laser engineered net shaping: Effects of deposition variables. Ceramics international 43, 7768–7775.

Mahmood. M.A., Popescu., A.C., Mihailescu, I.N., 2020. Metal matrix composites synthesized by laser-melting deposition: a review. Materials 2020, 13(11): 2593.

Xu, W., Lui, E.W., Pateras, A., Qian, M., Brandt, M., 2017. In situ tailoring microstructure in additively manufactured Ti-6Al-4V for superior mechanical performance. Acta Materialia 125, 390–400.

Bermingham, M.J., StJohn, D.H., Krynen, J., Tedman-Jones, S., Dargusch, M.S., 2019. Promoting the columnar to equiaxed transition and grain refinement of titanium alloys during additive manufacturing. Acta Materialia 168, 261-274.

Laoui, T., Santos, E., Osakada, K., Shiomi, M., Morita, M., Shaik, S.K., Tolochko, N.K., Abe, F., Takahashi, M., 2006. Properties of titanium dental implant models made by laser processing. Proceedings of the Institution of Mechanical Engineers, Part C 220, 857–863.

Hayat, M.D., Singh, H., He, Z., Cao, P., 2019. Titanium metal matrix composites: An overview. Composites Part A: Applied Science and Manufacturing 121, 418-438.

Huang, L.J., Geng, L., Peng, H.X., Balasubramaniam, K., Wang, G.S., 2011, Effects of sintering parameters on the microstructure and tensile properties of in situ TiBw/Ti6Al4V composites with a novel network architecture. Materials and design 32, 3347–3353.

Ding, L., Hu, S. Quan, X., Shen, J., Effect of aging treatment on microstructure and properties of VN alloy reinforced Co-based composite coatings by laser cladding. Materials Characterization 129, 80–87.

Hu, Y., Cong, W. Wang, X., Li, Y., Ning, F., Wang, H., 2018. Laser deposition-additive manufacturing of TiB-Ti composites with novel three-dimensional quasi-continuous network microstructure: Effects on strengthening and toughening. Composites Part B: Engineering 133, 91–100.

Niu, J., Dai, G., Guo, Y., Sun, Z., Dan, Z., Dong, Y., Chang, H., Alexandrov, I. V., Zhou, L., 2021. Microstructure and mechanical properties of B modified Ti–Fe alloy manufactured by casting, forging and laser melting deposition. Composites Part B: Engineering 216, 108854.

Cai, C., Radoslaw, C., Zhang, J., Yan, Q., Wen, S., Song, B., Shi, Y., 2019. In-situ preparation and formation of TiB/Ti-6Al-4V nanocomposite via laser additive manufacturing: microstructure evolution and tribological behavior. Powder Technology 342, 73–84.

Das, M. Balla, V.K., Basu, D., Bose, S., Bandyopadhyay, A., 2010. Laser processing of SiC-particle-reinforced coating on titanium. Scripta Materialia 63, 438–441.

Gu, D., Hagedorn, Y.C., Meiners, W., Wissenbach, K., Poprawe, R., 2011. Selective Laser Melting of in-situ TiC/Ti5Si3 composites with novel reinforcement architecture and elevated performance. Surface and Coatings Technology 205, 3285–3292.

Wang, T., Zhu, Y.Y., Zhang, S.Q., Tang, H.B., Wang, H.M., 2015. Grain morphology evolution behavior of titanium alloy components during laser melting deposition additive manufacturing. Journal of Alloys and Compounds 632, 505–513.

Roger, J., Gardiola, B., Andrieux, J., Viala, J.C., Dezellus, O., 2017. Synthesis of Ti matrix composites reinforced with TiC particles: thermodynamic equilibrium and change in microstructure. Journal of Materials Science 52, 4129–4141.

Sumida, M., Kondoh, K., 2005. In-situ synthesis of Ti matrix composite reinforced with dispersed Ti5Si3 particles via spark plasma sintering. Materials transactions 46, 2135–2141.

Lu, W., Zhang, D., Zhang, X., Wu, R., Sakata, T., Mori, H., 2001. Microstructural characterization of TiC in in situ synthesized titanium matrix composites prepared by common casting technique. Journal of Alloys and Compounds 327, 248–252.

Bramfitt, B.L., 1995. The effect of carbide and nitride additions on the heterogeneous nucleation behavior of liquid iron. Metallurgical Transactions 1, 1987–1995.

Huang, L.J., Geng, L., Li, A.B., Yang, F.Y., Peng, H.X., 2009. In situ TiBw/Ti-6Al-4V composites with novel reinforcement architecture fabricated by reaction hot pressing. Scripta Materialia 60, 996–999.